AGU PUBLICATIONS

JGR

Journal of Geophysical Research: Solid Earth

RESEARCH ARTICLE
10.1002/2015JB012619

Key Points:
- Evaluate Rayleigh and P_n waveforms predicted by six 3-D velocity models in Tibet and surrounding area
- Rigorous select ground truth seismic events to minimize the influence of uncertainties in sources
- Highlight the needs of jointly inverting body and surface waves as well as anisotropy for tomography

Supporting Information:
- Supporting Information S1

Correspondence to:
X. Bao,
xybao@uri.edu

Citation:
Bao, X., and Y. Shen (2016), Assessing waveform predictions of recent three-dimensional velocity models of the Tibetan Plateau, *J. Geophys. Res. Solid Earth*, *121*, 2521–2538, doi:10.1002/2015JB012619.

Received 23 OCT 2015
Accepted 15 MAR 2016
Accepted article online 23 MAR 2016
Published online 9 APR 2016

Assessing waveform predictions of recent three-dimensional velocity models of the Tibetan Plateau

Xueyang Bao[1] and Yang Shen[1]

[1]Graduate School of Oceanography, University of Rhode Island, Narragansett, Rhode Island, USA

Abstract Accurate velocity models are essential for both the determination of earthquake locations and source moments and the interpretation of Earth structures. With the increasing number of three-dimensional velocity models, it has become necessary to assess the models for accuracy in predicting seismic observations. Six models of the crustal and uppermost mantle structures in Tibet and surrounding regions are investigated in this study. Regional Rayleigh and P_n (or P_{nl}) waveforms from two ground truth events, including one nuclear explosion and one natural earthquake located in the study area, are simulated by using a three-dimensional finite-difference method. Synthetics are compared to observed waveforms in multiple period bands of 20–75 s for Rayleigh waves and 1–20 s for P_n/P_{nl} waves. The models are evaluated based on the phase delays and cross-correlation coefficients between synthetic and observed waveforms. A model generated from full-wave ambient noise tomography best predicts Rayleigh waves throughout the data set, as well as P_n/P_{nl} waves traveling from the Tarim Basin to the stations located in central Tibet. In general, the models constructed from *P* wave tomography are not well suited to predict Rayleigh waves, and vice versa. Possible causes of the differences between observed and synthetic waveforms, and frequency-dependent variations of the "best matching" models with the smallest prediction errors are discussed. This study suggests that simultaneous prediction for body and surface waves requires an integrated velocity model constructed with multiple seismic waveforms and consideration of other important properties, such as anisotropy.

1. Introduction

Thanks to advances in seismic data acquisition, seismic theory, and computation, numerous three-dimensional (3-D) Earth models have been generated and interpreted for Earth structures during the past decades. With the availability of multiple models inverted from different methods and data sets, it becomes important to evaluate the performance of the models on resolution and accuracy. A common approach in model assessment is to directly compare the observed waveforms with synthetics simulated with a given model [e.g., *Song and Helmberger*, 2007; *Lee et al*., 2014; *Maceira et al*., 2015]. Using 3-D full-wave simulation and ambient noise measurements, *Gao and Shen* [2012] systematically tested five surface wave tomographic models in the Cascades. A following study extended the validation for five shear wave velocity models that cover the western or entire contiguous United States and included waveforms from both ambient noise and regional earthquakes [*Gao and Shen*, 2015]. These validation studies showed that although the patterns of large-scale velocity anomalies in these models are similar, there are substantial differences in the magnitude of the velocity structure and the predicted waveforms.

A major motivation of this study is to assess whether models constructed from surface waves can be used to predict body wave arrivals, and vice versa. For various reasons, many velocity models are incomplete in the sense that they are compressional or shear velocity models constructed from *P*, *S*, or surface waves. For example, in places with few earthquakes, ambient noise tomography (and the resulting V_s model) might be the only affordable way to obtain a 3-D tomographic model of the crust and upper mantle. This is a basic question that must be answered for the utilization of 3-D velocity models, such as in earthquake location and source moment inversion.

Recently, several 3-D velocity models for the Tibetan Plateau have become publicly available. Unlike the United States, which is covered by numerous seismic stations, Tibet is an area with a relatively poor coverage of seismic networks. This is likely one of the main reasons of the large disagreements observed among the different models of Tibet (Figures 1 and 2). This kind of disagreements among the models is likely representative of areas outside of the United States and other areas with dense station coverage. Unlike *Gao and Shen* [2012, 2015], which focused on surface waves only, our attention in this study is on P_n (or P_{nl} at long periods)

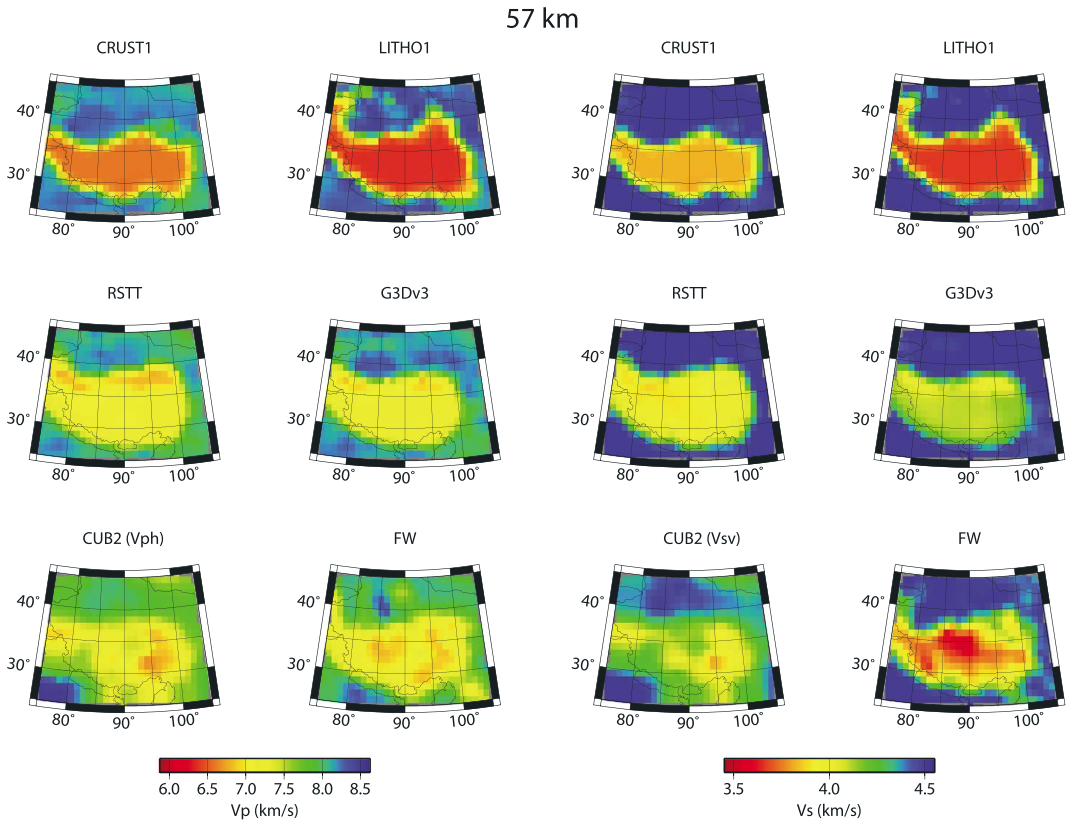

Figure 1. The models selected for validation in this study at the depth of 57 km, in (first and second columns) V_p and (third and fourth columns) V_s.

as well as regional Rayleigh waves to validate both compressional and shear velocities of the six global or regional 3-D Earth models for Tibet and its surrounding regions. In addition, we follow a rigorous selection of ground truth seismic events to minimize uncertainties in the seismic sources. We use a 3-D finite-difference forward modeling method to assess the accuracy of the six 3-D velocity models in Tibet in predicting both Rayleigh and P_n/P_{nl} waveforms. In the following, we briefly introduce these velocity models in section 2 and describe the data and the measuring technique for model validation in sections 3 and 4, respectively. We then discuss the success and failure of the models constructed with surface waves in predicting P_n/P_{nl}, and vice versa, as well as the possible causes of prediction errors (e.g., radial anisotropy and V_p/V_s ratio).

2. Models

Six 3-D velocity models, including five global models and one subhemisphere model, are used in this validation. The parameters V_p, V_s, and density are required in a 3-D model in order to simulate full-wave propagation.

The global model *CRUST1.0* was based on CRUST2.0 with new constraints such as recent active source experiments and receiver function studies [*Laske et al.*, 2013]. In this isotropic model, each $1° \times 1°$ cell includes eight layers in the crust and a mantle layer. For the crust, it gives topography (or bathymetry), V_p, V_s, and density in each layer and the depth of each layer's bottom. Below the Moho discontinuity, the mantle parameters in CRUST1.0 do not change in the vertical direction.

LITHO1.0 is a $1° \times 1°$ model of the crust and mantle lithosphere [*Pasyanos et al.*, 2014]. It was constructed by inverting fundamental-mode Love and Rayleigh wave phase and group velocities in the period band of 25–200 s. Constraints from CRUST1.0 and LLNL-G3Dv3 (section 2.4) were employed to set up the starting model in the inversion for LITHO1.0. This model provides V_p, V_s, and density in eight crustal layers and two layers beneath the Moho for the mantle lithosphere and asthenosphere, respectively.

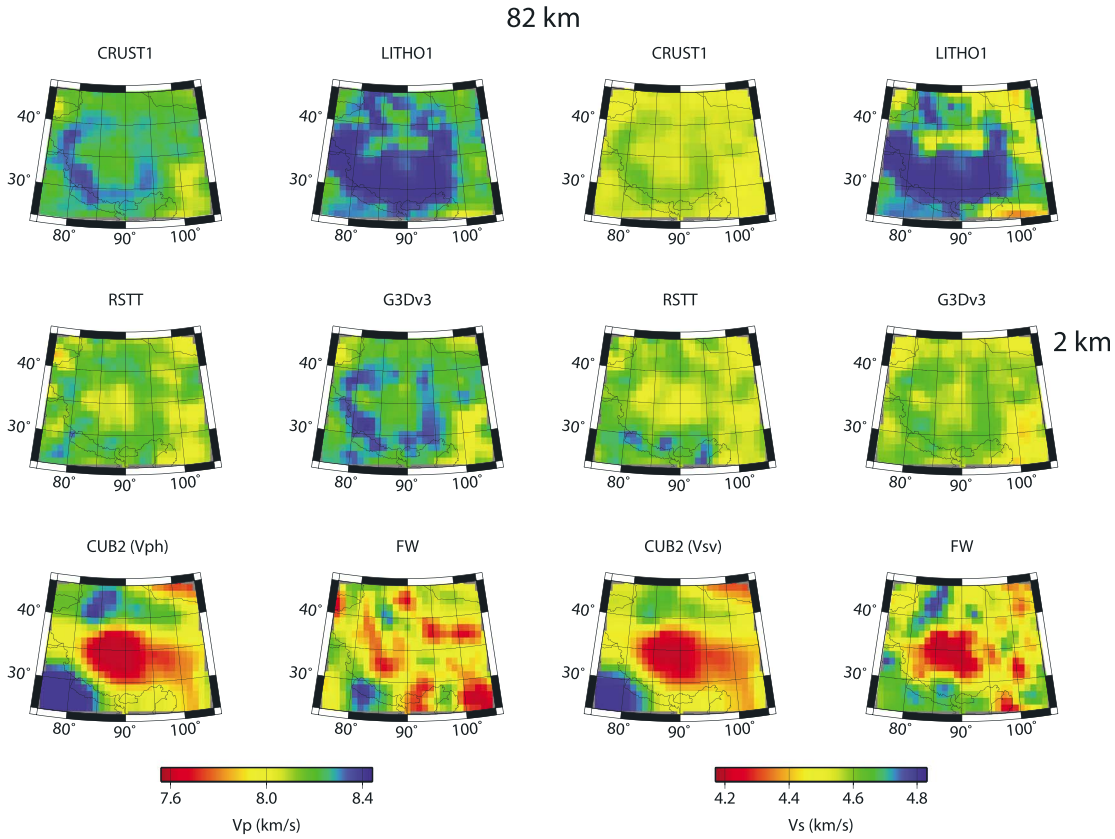

Figure 2. As in Figure 1 but for the depth of 82 km.

RSTT is a V_p and V_s model for the 3-D crust and laterally variable uppermost mantle generated by using regional *P* and *S* traveltime data [e.g., *Myers et al*., 2010]. To account for the fact that P_n and S_n waves do not travel purely horizontally like the classic head wave, the inversion included an additional term to describe vertical velocity gradients in the uppermost mantle as suggested by *Zhao and Xie* [1993]. RSTT includes seven layers in the crust and a mantle layer with a uniform positive vertical velocity gradient at individual horizontal grids. Since V_p and V_s are inverted separately, V_p/V_s ratios are not constant in the model. The density is estimated by employing the empirical relation between V_p and density [*Christensen and Mooney*, 1995].

The global *P* wave velocity model LLNL-G3Dv3 (hereinafter *G3Dv3*) was developed by using *P* and P_n arrival time data, 3-D ray tracing, iterative inversion, and source relocation with Bayesian analysis [*Simmons et al*., 2012]. Within the data used in tomography, the percentage of P_n measurements is approximately 10%. The starting model in the inversion for G3Dv3 included information in RSTT. A recent study investigated the accuracy of G3Dv3 by applying a 3-D ray tracing to the prediction of *P* wave arrival time [*Myers et al*., 2015]. This model consists of 57 layers from the surface to the core-mantle boundary. The Earth's ellipticity has been taken into consideration in the model. We assume that V_s at a given depth can be estimated from V_p by employing the empirical V_p/V_s ratio of 1.74 for the crust [*Brocher*, 2005] and the V_p/V_s ratio of AK135 [*Kennett et al*., 1995] for the mantle. Density is estimated by the same method as for RSTT.

The global shear wave velocity model *CUB2.0* was tomographically determined by using fundamental-mode Love and Rayleigh wave group and phase velocity data [*Shapiro and Ritzwoller*, 2002]. This $2° \times 2°$ radially anisotropic model describes V_s, V_{sh}, and V_{sv} in the upper mantle down to 396 km depth with a uniform depth grid of 4 km. We select the version of this model inverted based on a simplified version of scattering sensitivity kernels [*Ritzwoller et al*., 2002]. The same assumption of V_p/V_s ratios used to set up the finite-difference model of G3Dv3 is applied to convert V_{sv} and V_{sh} to V_{pv} and V_{ph}, respectively, for simulations for Rayleigh and P_n/P_{nl} waves. This is because Rayleigh wave phase velocity is mainly determined by V_{sv}, and the velocity of P_n/P_{nl} is

Table 1. Six 3-D Global or Regional Velocity Models Used in This Validation[a]

Model Name	V_p	V_s	ρ	Data Used for Original Model	Model Format
CRUST1.0	Yes	Yes	Yes	*P* waves (e.g., active source studies and receiver functions), gravity, etc.	Layered
LITHO1.0	Yes	Yes	Yes	Surface waves	Layered
RSTT	Yes	Yes	No	Regional *P* and *S*	Layered
G3Dv3	Yes	No	No	*P* and P_n	Layered
CUB2.0	No	Yes, anisotropic	No	Surface waves	Grid
FW	Yes	Yes	Yes	Ambient noise	Grid

[a]The availability of the parameters of V_p, V_s, and density (ρ) given by a model in the public version is marked by yes or no. For example, G3Dv3 provides only V_p of the three parameters. The types of data used in the inversion for a model are listed, as well as the types of the model structure, in layer or in grid.

mostly sensitive to V_{ph} since they travel nearly horizontally in the mantle. We estimate the density by using the same conversion as for RSTT and G3Dv3.

FW is a full-waveform tomography model based on a scattering-integral method [*Shen and Zhang*, 2012]. This full-wave shear velocity model was generated by inverting intermediate- to long-period (12.5–600 s) empirical Green's functions extracted from ambient seismic noise [*Shen et al*., 2012]. The model is a fine-grid 3-D V_p, V_s, and density model from the surface to the lower mantle. The grid interval increases with depth from 7 km at the top to about 50 km at 1900 km depth. This subhemispheric model covers the area approximately between the latitude (55°S, 55°N) and the longitude (30°W, 156°E).

The basic differences in these models are highlighted in Table 1. The six models of V_p and V_s are compared at depths of 57 km and 82 km in Figures 1 and 2, respectively. There are significant differences in V_p and V_s among these models at each depth. Notice that the crust of Tibet can be up to 80 km thick, with an average thickness larger than 60 km, and the Moho of the surrounding regions is generally shallower than 50 km depth [e.g., *He et al*., 2014; *Li et al*., 2014]. The maps of Moho topography of the models are shown in supporting information Figure S1. At 57 km depth, the basic pattern of low V_p and V_s of the Tibetan lower crust is consistent among the models, but the magnitudes of V_p and V_s structures vary in different models. For example, the values of V_p in Tibet of CRUST1.0 and LITHO1.0 are more than 0.5 km/s lower than those in other models, where LITHO1.0 has extremely low V_p ($<$6.4 km/s) in the Tibetan lower crust. The other five models exhibit consistent lower crustal V_p of about 7 km/s in Tibet. In addition, the minimum value of V_p is located in different places in different models: the northern plateau in RSTT and G3Dv3, the eastern plateau in CUB2.0, and the central and the eastern plateau in FW. In areas surrounding Tibet, V_p in the upper mantle also varies in different models. For instance, LITHO1.0 has a faster V_p north of Tibet than other models. The major patterns of V_s models are similar to those of V_p models, except FW, which also exhibits a pronounced low V_s in the lower crust of Tibet. At 82 km depth, V_p and V_s in the mantle of Tibet and surrounding region differ more significantly among the models than at 57 km depth. The four layered models (CRUST1.0, LITHO1.0, RSTT, and G3Dv3) have on average higher V_p and V_s velocities than CUB2.0 and FW. In particular, the layered models, except RSTT, have V_p and V_s larger than the corresponding values of the global average (AK135): 8.04 km/s for V_p and 4.49 km/s for V_s. In contrast, CUB2.0 and FW have significantly low velocities in the uppermost mantle of the northern and central Tibetan Plateau. Overall, unlike the models for the western United States compared by *Gao and Shen* [2015], the lateral patterns of the six velocity models of Tibet and the vicinity are significantly different, especially for the upper mantle.

3. Data

Model validation generally needs to address two important issues on data selection: the uncertainty and independence of the data.

First, synthetic seismograms based upon a model are typically compared to corresponding observations. So ideally, the differences between synthetic and observed seismograms are caused only by the differences between structures in the model and the real Earth where waves propagate. This requires accurate event location and origin time determination. To minimize location and origin time uncertainties, we use the ground truth (GT) events determined with rigorous criteria [*Bondár et al*., 2004]. These GT events are divided into different groups according to the epicenter location accuracy. The global GT reference event catalog

Table 2. The Two Representative GT Events Selected From the Two Clusters Found Available in the Region[a]

	Event Name	
	1992142	1999087
Origin time[b]	1992/05/21 04:59:59.9	1999/05/28 19:05:11.5
Latitude (deg)	41.5437	30.4940
Longitude (deg)	88.7641	79.3470
Depth (km)	0	12
GT level	1	7
m_b	6.5	6.4
Half duration (s)	0	4.7
Moment (dyne cm)	26	25
M_{rr}	1	1.579
M_{tt}	1	−1.826
M_{pp}	1	0.247
M_{rt}	0	6.843
M_{rp}	0	−3.180
M_{tp}	0	0.843

[a]The half-time duration is used to estimate source time function. Event 1992142 is assumed to be a pure explosive source with an arbitrary moment magnitude as we are interested only in traveltimes. The moment tensor and half duration of Earthquake 1999087 are from the Global CMT solution.
[b]Dates are formatted as year/month/day.

(International Association of Seismology and Physics of the Earth's Interior) is available at the International Seismological Centre. It is challenging to find appropriate data for our validation for four reasons. First, only a few GT events can be found in continental Asia due to the lack of good publicly available seismic network coverage to satisfy the geometrical criteria in the determination of GT events. Second, data selection is further limited by the lack of seismic stations in Tibet at the times of the few GT events. Third, the full-waveform validation analysis requires estimation on the source mechanism for waveform simulation, which is generally not a concern in GT catalogs. We thus have to find overlapping events between the GT catalogs, which provide the source hypocenter location and origin time, and the Global Centroid Moment Tensor catalog (GCMT) [*Ekström et al.*, 2012], which gives the source moment tensor as well as the source time duration. Such overlap is not typical because GT events are usually not large earthquakes, while it is opposite in the GCMT catalog. Fourth, an event identified by both the GT catalog and GCMT may still be unusable because of low signal-to-noise ratios. After a thorough search and quality control, we find two GT event clusters in the neighborhood of Tibet: one underground explosion cluster and one earthquake cluster (Table 2). The largest event (in m_b) in each cluster is selected as the representative for the cluster. Event locations are illustrated in Figure 3, along with the available broadband stations and corresponding great-circle ray paths.

Event 1992142 was the largest explosion in m_b in a cluster that includes eight $m_b > 5.6$ GT events since 1990. This event was recorded at seven stations in the 1991–1992 Incorporated Research Institutions for Seismology (IRIS)-Portable Array Seismic Studies of the Continental Lithosphere Tibetan Plateau temporary broadband seismic network. Five stations were deployed along the Lhasa to Golmud transect in the plateau, including station TUNL near the southern edge of the Qaidam Basin. Two other stations were located in the eastern Tibetan Plateau. Epicentral distance ranges from 792 to 1275 km. Event 1999087 is the main shock of an M_w 6.5 earthquake that occurred in the Chamoli district (India) in the Himalaya. This earthquake was recorded by the dense passive-source seismic array INDEPTH-III, which was deployed in central Tibet across the Bangong-Nujiang Suture (BNS) from the Lhasa terrane to the Qiangtang terrane during 1998–1999. The major part of this network was designed as a nearly NW-SE profile. The epicentral distances are between 922 and 1034 km, generally increasing from north to south.

The second consideration for the data used for validation is that they should ideally not be used as input when the model was established. The models tested in this study, except the G3Dv3 and RSTT, were inverted from surface waves measurements, which means that P_n was not used as constraint for those models. The P_n measurements used for G3Dv3 occupied less than 10% of the entire P wave data set, which suggests that P_n is not the only constraint for this velocity model beneath Tibet. A validation test for RSTT [*Myers et al.*, 2010] has included one GT event from each cluster used in this study. Conversely, Rayleigh waves used in this study are independent of the P and P_n used to build G3Dv3 and RSTT. The data used in this study were not included in the generation of FW.

4. Method

4.1. Waveform Simulation

For each event and Earth model, wave propagation is simulated with a collocated-grid finite-difference method in the spherical coordinates [*Zhang et al.*, 2012]. The algorithm can achieve high-order precision by avoiding the

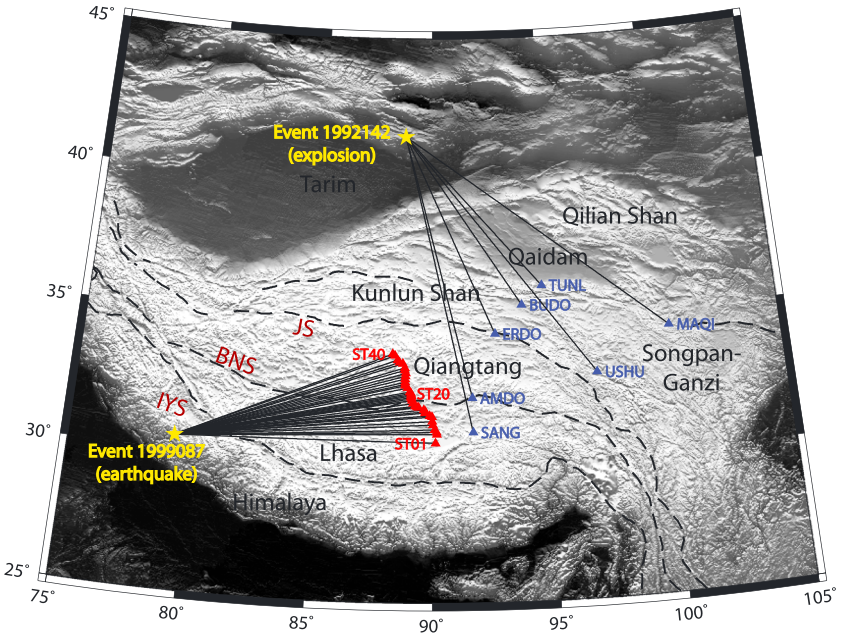

Figure 3. A map of events (yellow stars), stations (blue triangles for Event 1992142 and red triangles for Event 1999087), and corresponding great-circle ray paths (black lines) on the background of surface topography. Dashed lines are major tectonic sutures. The two yellow stars represent the source epicenters. Station names are labeled in blue for Event 1992142 and red for Event 1999087 (only at three representative stations in the dense profile, where ST20 is where the profile crossed the BNS). IYS: Indus-Yalung suture, BNS: Bangong-Nujiang suture, JS: Jinsha suture.

interpolation on particle velocity and stress typically used in classic staggered grid finite-difference method. It includes a complex frequency-shifted perfectly matched layer absorbing boundary implemented through auxiliary differential equations. The finite-difference codes have been verified against the normal mode solutions and have been demonstrated to produce excellent fit of body and surface waves [*Zhang et al*., 2012]. *Gao and Shen* [2015] used this method to simulate regional Rayleigh waves and empirical Green's functions extracted from ambient seismic noise at multiperiod bands from 15 to 75 s. To further verify the finite-difference method for 3-D models at the scales of the study area, we compared the waveforms from our finite-difference simulations with the available synthetics calculated from the spectral element method (SEM) synthetics in the 3-D synthetics database at the IRIS Data Management Center (*Tromp et al*. [2010], ShakeMovieSynthetics). We find that the finite difference and SEM synthetics match well (supporting information Figures S4 and S5), indicating that the validation results discussed below do not depend on whether the finite-difference method [*Zhang et al*., 2012] or the SEM [*Komatitsch and Tromp*, 2002] are used. The small difference in the synthetics is likely due to differences in the discretization of the same 3-D model and probably different V_p/V_s ratios and V_p-density relationships.

We use two ways to implement the velocity models in the 3-D finite-difference grids (Table 1). For a layered model, which has interface topography and lateral variations in parameters in each layer, a polynomial interpolation along the vertical direction within each layer is used to set up the values of parameters at each grid between the top and bottom of the layer. For a model with 3-D grid points, the medium parameters for each finite-difference grid are interpolated from the corresponding values in the model. The grids are shifted downward by an amount equal to the surface elevation to create a flat surface used by the finite-difference method of *Zhang et al*. [2012].

The source types of the two GT events are distinctly different (Table 2). For the explosion, we assume that the explosion occurred over a short enough time that it can be treated as instantaneous, and thus we use a Heaviside step function to represent its source time function. For the earthquake, a Bell integral step function is used to describe the time function at the source, where the half duration of the source time function is employed from GCMT.

Our objective is to validate the Earth models by using both Rayleigh waves and P_n/P_{nl} waves. To save computational cost, we choose different grid spacings and wave propagation times for Rayleigh waves and P_n/P_{nl} waves. The lateral grid spacings are ~0.025° for regional Rayleigh waves and ~0.01° for P_n/P_{nl} waves. The vertical grid

spacing increases with depth. For P_n/P_{nl} wave simulation, the grid size is ~0.37 km near the surface, ~2 km at 100 km depth, and ~3 km at 200 km depth. The maximum depths for simulation are 500 km for Rayleigh waves and 200 km for P_n/P_{nl} waves. To satisfy the numerical stability condition, the time intervals are 0.15 s and 0.05 s for Rayleigh and P_n/P_{nl} wave simulations, respectively. The corresponding time window lengths of 750 s for Rayleigh waves and 300 s for P_n/P_{nl} are estimated from the maximum epicentral distance. Based on the grid spacing selected in the simulations, the shortest usable periods are approximately 15 s and 1 s for synthetic Rayleigh and P_n/P_{nl} waves, respectively. Because the source-receiver paths for these two events are in different parts of the study area, we use different simulation boxes for the two events for computational efficiency.

The effect of intrinsic attenuation on the traveltimes of short-period Rayleigh waves and P_n/P_{nl} waves is assumed to be minor and thus not considered. The influence of anisotropy is not simulated in the full-wave sense. Since the model CUB2.0 incorporates radial anisotropy of shear wave velocity in the mantle, we separately simulate Rayleigh and P_n/P_{nl} waves through the models of V_{sv} and V_{sh} given by CUB2.0, respectively (more discussion in section 6). Surface topography typically affects the waveform of *P* coda at periods shorter than the shortest period simulated here [*Rodgers et al*., 2010] and thus is ignored as well. Because the source-receiver distances in this study are much greater than the surface elevation, the downward shift of grids by the amount of surface elevation has little to no effect on Rayleigh or P_n wave traveltimes.

4.2. Cross Correlation Between Synthetic and Observed Waveforms

The observed seismograms and instrument responses of all stations that recorded the events are requested from the IRIS Data Management Center. Instrument responses are removed from the raw seismograms, which are then transferred into velocity seismograms. The event locations and origin times are adopted from the GT catalog (Table 2). We apply a zero-phase Butterworth band-pass filter on the observed seismograms and then manually pick the approximate windows of Rayleigh waves and P_n/P_{nl} waves. Appropriate window lengths are determined empirically, taking into consideration the distances, filter frequencies, and the quality of signal. We select two period bands for regional Rayleigh waves: 20–50 s and 35–75 s. For P_n/P_{nl}, four-period bands, including 10–20 s, 5–10 s, 2–5 s, and 1–2 s, are tested. The two longer periods (10–20 s and 5–10 s) with longer window lengths represent P_{nl} phases; the two short periods (2–5 s and 1–2 s) with shorter window lengths represent P_n. The same band-pass filter and window lengths are used to process synthetic seismograms. For synthetic seismograms, we use the TauP package [*Crotwell et al*., 1999] to predict a rough P_n arrival time based on the AK135 model. Depending on the distance and frequencies, the start of the synthetic phase window is determined with respect to the TauP prediction, which can be manually shifted in case of very early or late synthetic arrivals relative to the observed. The window for synthetic Rayleigh waves is the same as the picked window on the observed seismograms. A Tukey window is used to taper the first and last 25% of the samples in the phase window. The time delay is measured at the point where the cross-correlation function has a global maximum. To minimize cycle skipping, particularly for high-frequency P_n, a manual treatment is carried out after the automated correlation by visually comparing the waveforms at nearby stations. After shifting the synthetic phase window with the optimal time shift obtained from the cross-correlation function, we then calculate the cross-correlation coefficient between synthetics and observations.

Because the simulation is in a spherical coordinate while the real Earth is an ellipsoidal volume, the effect of ellipticity needs to be corrected. For example, the spherical distance and ellipsoidal distance between Explosion 1992142 and station SANG are 1198.8 and 1196.5 km, which may yield a traveltime difference of ~0.6 s and ~0.3 s in Rayleigh and P_n wave arrivals, respectively. We correct the effect of ellipticity by multiplying the time scale of the observed waveforms by a ratio between the spherical and ellipsoidal distances. Then a procedure of resampling at 0.01 s intervals is executed on both the observed and synthetic phase windows.

Signal-to-noise ratios are calculated to exclude those seismograms with high background noise. The ratios at low frequencies are generally lower than those at higher frequencies. Different thresholds of signal-to-noise ratio are chosen for different frequency bands: 10 for Rayleigh waves, 2 for 10–20 s and 5–10 s P_n/P_{nl}, and 10 for 2–5 s and 1–2 s P_n/P_{nl}. Poor signals are common for P_n/P_{nl} at 10–20 s period for Explosion 1992142, so we decide not to measure the time delay for this group of data.

Five examples of the phase delay measurements of Rayleigh and P_n/P_{nl} waves for Event 1992142 and station AMDO at all period bands are shown from Figures 4–8. Each figure includes the comparison between the observed (black) and synthetic waveforms (red) for the six models. The synthetic waveform amplitudes are normalized

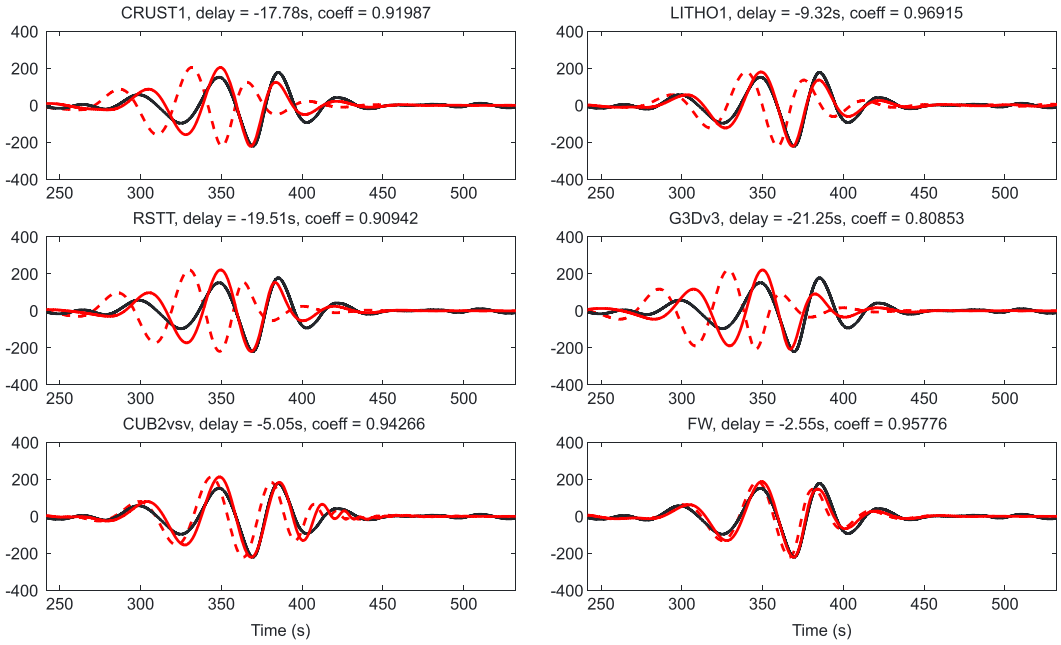

Figure 4. Observed (black) Rayleigh waveforms of the Event 1992142 (explosion) recorded by station AMDO are compared with the synthetics for the six models before (red dashed) and after (red solid) time shifts by the phase delays noted in the subtitles. The waveforms have been filtered in 35–75 s period. The observed and synthetic waveforms have identical phase windows, shown as the length of each figure. The values of correlation coefficients, also listed in the subtitles of all figures, are calculated by comparing the observation and shifted synthetic waveforms. The synthetic waveform amplitudes are normalized according to the maximum amplitude in the phase window of the real data.

according to the maximum amplitude in the phase window of the real data. Examples of Rayleigh waves (35–75 s) and P_n/P_{nl} waves (5–10 s) for Event 1999087 (earthquake) are displayed in Figures S2 and S3, respectively.

Compared to explosion data, additional care must be taken in the use of earthquakes for model validation because of earthquake location errors and the more complex source time function. First, since Earthquake 1999087 has a half-time duration of 4.7 s and the source time function used in simulations is a Bell integral

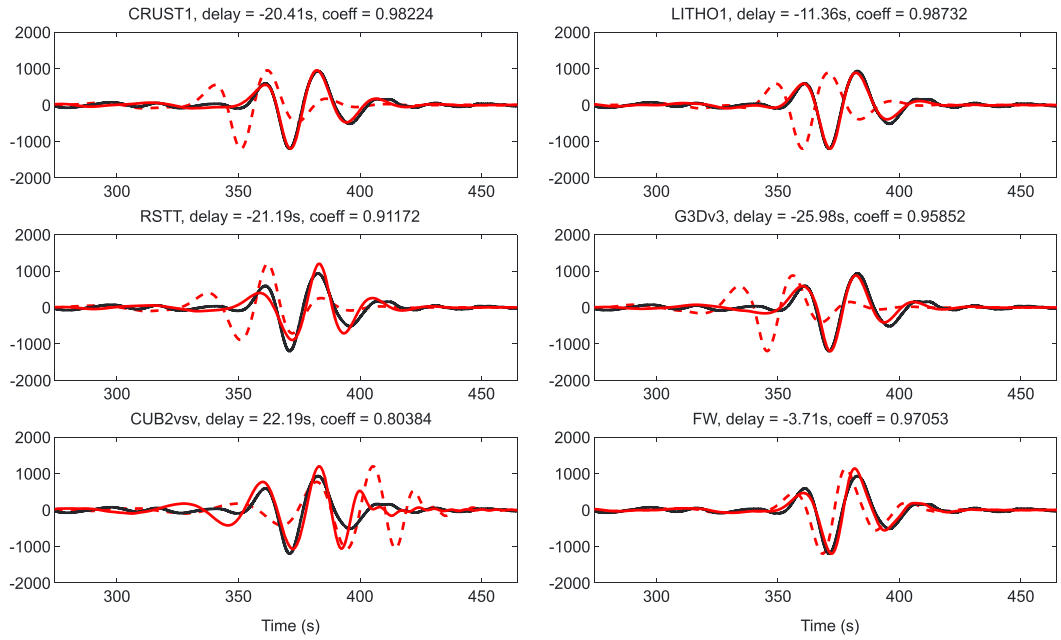

Figure 5. As in Figure 4 but for Rayleigh waves filtered at 20–50 s period.

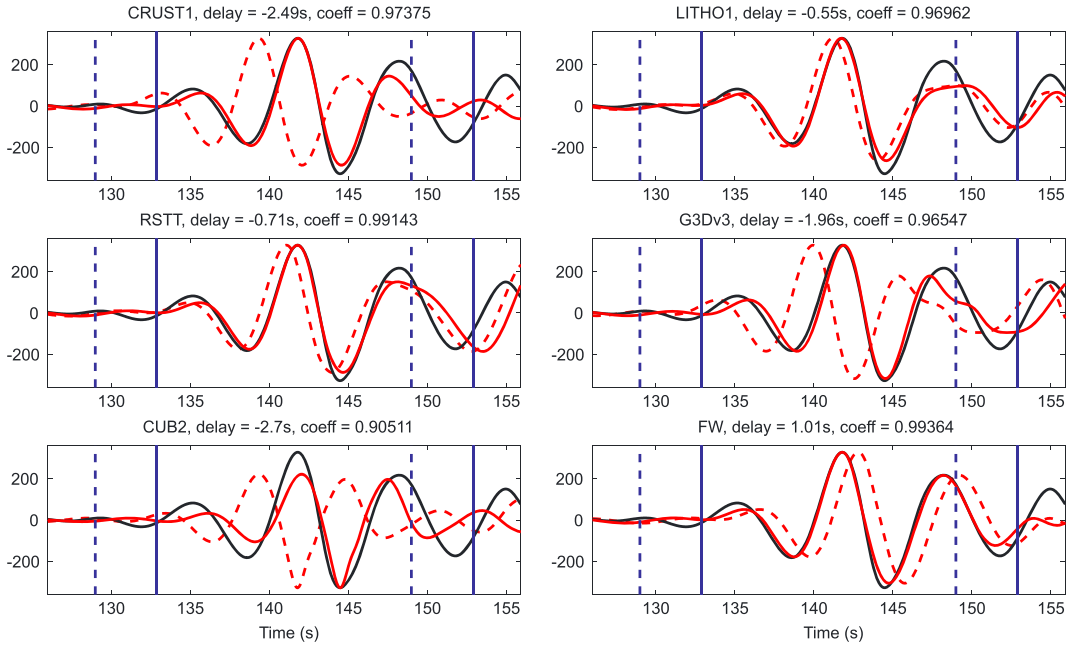

Figure 6. As in Figure 4 but for P_n waves filtered at 5–10 s period. The windows with solid blue and dotted blue edges are the windows manually picked for the observed waveforms and the predicted by the TauP Toolkit for the synthetic waveforms.

step function, the short-period waves of the synthetics likely do not represent the complexity in the source time function for this earthquake. In general, small initial wavelets are visible in the observed waveforms before the largest P_n phase (Figure S3). Such waveform complexity is not simulated by using a simple source time function. A detailed study modeling the source time function of this earthquake is beyond the scope of this study. Therefore, the P_n phase measurements for this earthquake are limited to the longer-period P_{nl} (5–20 s) and Rayleigh waves. At these periods, waves are not strongly influenced by the source time complexity, though a delayed prominent onset in the real source time function relative to that used in simulation may result in an earlier phase prediction in synthetic seismograms. Second, this earthquake is listed in a GT7 catalog, unlike

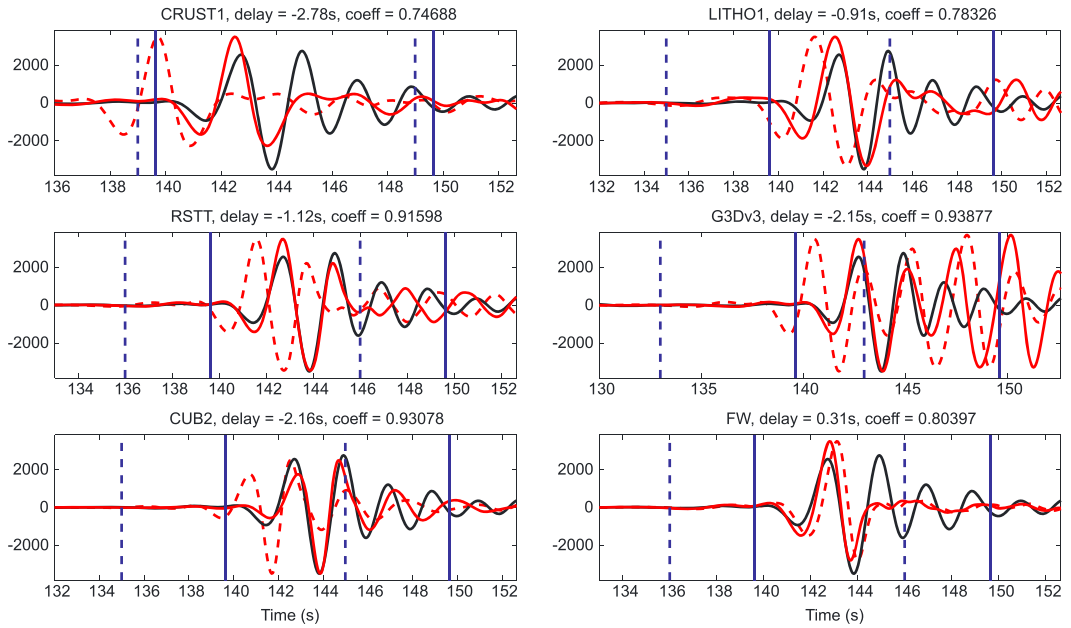

Figure 7. As in Figure 6 but for P_n waves filtered at 2–5 s period.

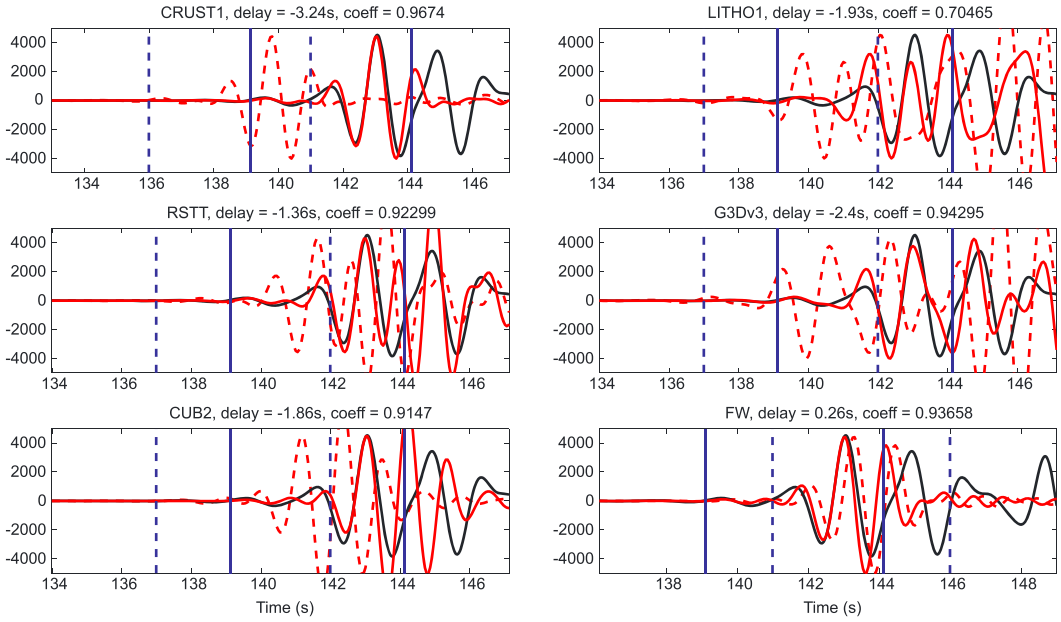

Figure 8. As in Figure 6 but for P_n waves filtered at 1–2 s period.

the explosion in a GT1 catalog, where the numbers after GT represent the location accuracy in kilometer. Previously estimated source locations of earthquakes in this region [*Satyabala and Bilham*, 2006] are typically aligned in approximately the west-northwestern-to-east-southeastern (WNW-ESE) direction, while the wave propagated to all INDEPTH-III stations with an azimuthal range of 64°–86° (from north to south along the profile). If the earthquake occurred on a fault with a WNW-ESE strike, the mislocation may cause errors of up to ±0.8 s for P_n waves and approximately ±1.7 s for 20–75 s Rayleigh waves. The depths provided in the major catalogs vary from 11 to 15 km. We use the depth given by the GT7 catalog (12 km) and note that the uncertainty in the source depth may result in up to 0.46 s delay in the predicted P_n (estimated by using crustal velocity of 6.5 km/s). The small effect of source depth uncertainty on the Rayleigh wave arrival times is ignored.

We focus on traveltimes and cross-correlation coefficients between the observed and synthetics in this study, and the waveform amplitude is not considered here for three reasons. First, none of the velocity models comes with a self-consistent intrinsic attenuation structure. Second, at short periods, waveform amplitudes may strongly depend on scattering associated with small-scale structures, such as thin layers in the mantle lid. Such small-scale structures have not been well modeled yet. Third, the source moment and site amplification may introduce further uncertainties. Instead, we seek to compare the relatively more robust measures of the waveforms, traveltimes and cross-correlation coefficients. In other words, the model prediction and validation reflect only the large- and intermediate-size velocity structures in the crust and uppermost mantle.

5. Results

5.1. Event 1992142: Explosion

For this event, the phase delays and correlation coefficients are measured at all seven stations for Rayleigh waves at 20–50 s and 35–75 s period, P_{nl} at 5–10 s period and 2–5 s period, and P_n at 1–2 s period. The phase delay measurements are hereinafter converted to slowness perturbation

$$\Delta s = -\frac{\Delta\tau}{d} = -\frac{\tau_{\mathrm{syn}} - \tau_{\mathrm{obs}}}{d}, \tag{1}$$

where $\Delta\tau$ is the phase delay, d the great-circle path epicentral distance, and τ_{syn} and τ_{obs} the phase traveltime in synthetics and observations, respectively. Figure 9 shows a comparison of the slowness perturbation and correlation coefficients in all the cases of this explosion. Unlike Δs, the correlation coefficients are sensitive to the selection of phase window. Hence, the value of Δs is considered as the primary parameter in the validation, and correlation coefficients could be supplementary especially when similar values of Δs are observed with respect to different Earth models.

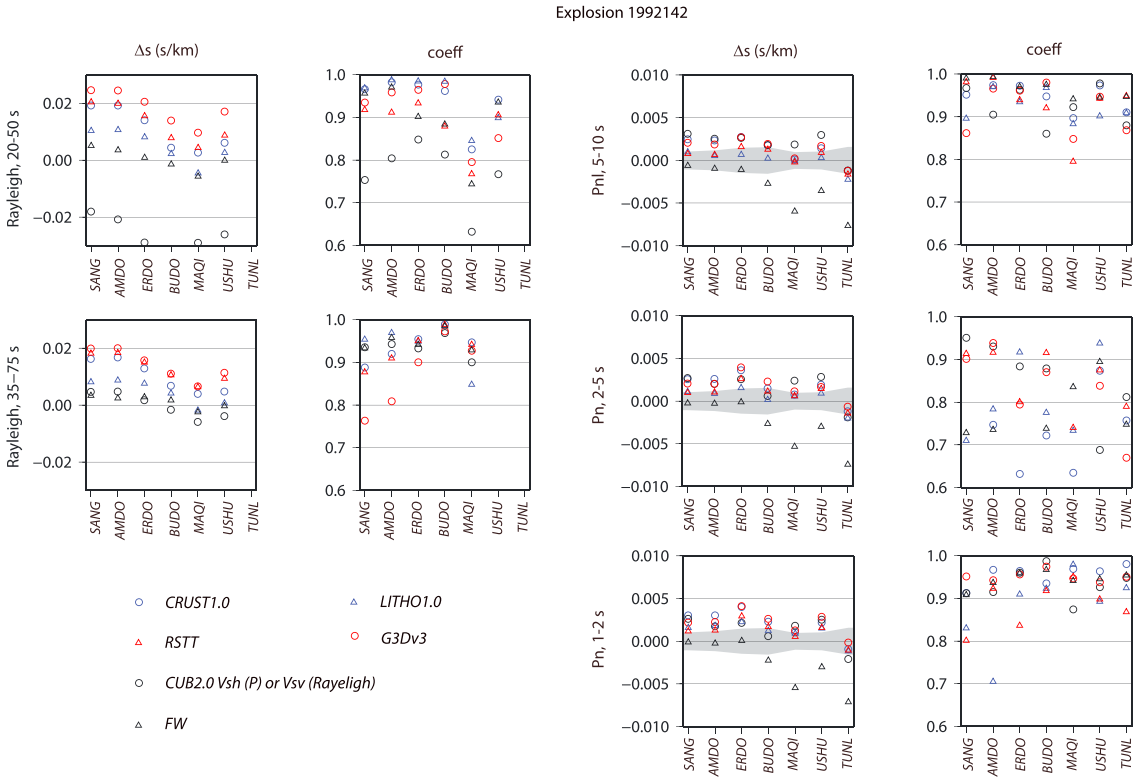

Figure 9. Slowness perturbations (Δs) and cross-correlation coefficients for Event 1992142. Δs and correlation coefficients of (first and second columns) Rayleigh waves and (third and fourth columns) P_n/P_{nl}. Figure 9 (first and second columns) is for Rayleigh waves at periods of (top) 20–50 s and (bottom) 35–75 s; Figure 9 (third and fourth columns) is for P_n/P_{nl} waves at periods of (top) 5–10 s, (middle) 2–5 s, and (bottom) 1–2 s. Positive Δs means fast models, and negative Δs means slow models. The model with symbol closest to the zero line is considered the best matching model for the given station, period, and phase. For P_n/P_{nl} waves, the gray areas show the corresponding GT10 thresholds used to determine matching models. The signal-to-noise ratios for station TUNL are lower than the threshold for Rayleigh waves; therefore, the corresponding measurements are not shown here.

At periods of 20–50 s and 35–75 s, Rayleigh waves mainly sample the Tibetan middle and lower crust and uppermost mantle. FW yields the best predictions with the smallest $|\Delta s|$ at most stations in both period bands. There is a major difference in the patterns of the phase delays for 20–50 s and 35–75 s period Rayleigh waves for CUB2.0 (V_{sv}). At periods of 20–50 s, predicted Rayleigh wave arrivals for CUB2.0 (V_{sv}) are slow at all stations. In contrast, the model produces small $|\Delta s|$ ($<$0.005 s/km) at 35–75 s, indicating that the mismatch is mainly caused by the velocity in the middle crust of CUB2.0. The models CRUST1.0, LITHO1.0,

Table 3. A Summary of the Best Matching Models for Rayleigh Waves at Periods of 20–50 s and 35–75 s From Both Event 1992142 and Event 1999087[a]

		Best Matching V_s Models	
Terrane	Station	20–50 s	35–75 s
Lhasa	SANG	FW	FW
	AMDO	FW	FW
	XR-South	FW	FW
Qiangtang	XR-North	FW	FW
	ERDO	FW	CUB2.0 (V_{sv})
Songpan-Ganzi	BUDO	FW	CUB2.0 (V_{sv})
	MAQI	CRUST1.0	LITHO1.0
	USHU	FW	FW
Qaidam	TUNL	N/A	N/A

[a]For Event 1999087, the INDEPTH-III station profile is separated by the BNS into the southern and northern portions, labeled as XR-South and XR-North (XR is the IRIS network code for INDEPTH-III). No best matching model is determined for station TUNL for its low signal-to-noise ratios.

Table 4. A Summary of the Models Within the GT10 Threshold for P_n/P_{nl} From Explosion 1992142 at Periods of 1–2 s, 2–5 s, and 5–10 s[a]

		V_p Models in GT10 Threshold		
Terrane	Station	1–2 s	2–5 s	5–10 s
Lhasa	SANG	**FW**	**FW** RSTT	**FW** RSTT LITHO1.0
	AMDO	**FW**	**FW** LITHO1.0 RSTT	**FW** LITHO1.0 RSTT
Qiangtang	ERDO	**FW**	**FW**	**LITHO1.0** FW
Songpan-Ganzi	BUDO	**CUB2.0 (V_{sh})** LITHO1.0	**LITHO1.0** CUB2.0 (V_{sh}) RSTT CRUST1.0	**LITHO1.0** RSTT
	MAQI	**RSTT** LITHO1.0	**RSTT** LITHO1.0 CRUST1.0	**CRUST1.0** LITHO1.0 RSTT G3Dv3
	USHU	No available model	**LITHO1.0**	**LITHO1.0** RSTT
Qaidam	TUNL	**G3Dv3** CRUST1.0 RSTT LITHO1.0	**G3Dv3** CRUST1.0 RSTT	**CUB2.0 (V_{sh})** CRUST1.0 G3Dv3 RSTT

[a]The model predicting the smallest $|\Delta s|$ is marked in boldface. The V_p model for CUB2.0 is converted from its V_{sh} component.

RSTT, and G3Dv3 are typically fast for Rayleigh, especially at the three stations in the Lhasa and Qiangtang terranes (SANG, AMDO, and ERDO). G3Dv3, constructed from *P* wave traveltime measurements, seems too fast for predicting Rayleigh waves. More than 90% of the cross-correlation coefficients are larger than 0.8 for Rayleigh waves of this event. The best matching models with the smallest $|\Delta s|$ for Rayleigh waves are summarized in Table 3.

Unlike Rayleigh waves, the pattern of P_n/P_{nl} slowness perturbations does not change substantially within the wave period used in this study. The change of Δs with periods from 1 to 10 s is typically smaller than 0.001 s/km (Figure 11, blue lines). More about the variation in Δs of P_n/P_{nl} as a function of the period is discussed in section 6.1. To place Δs in perspective, we introduce a threshold of Δs for P_n/P_{nl} that reflects the predicted uncertainty level of source location based on a given velocity model,

$$\Delta s_c = d_{GT}/dv_0, \tag{2}$$

where d_{GT}, d, and v_0 are the GT accuracy level, the great-circle path epicentral distance, and the empirical phase velocity, respectively. For example, d_{GT} is 10 km if a source is expected to be located within a GT10 level. To facilitate discussion, we define a model with the measured Δs smaller than the GT10 threshold as a matching model.

We seek the models within the GT10 threshold by checking whether the value of $|\Delta s|$ of a given model is between $\pm \Delta s_c$, which is generally in a range of 0.002–0.003 s/km. Table 4 lists the models with predictions within the GT10 threshold for this event. FW is typically a slow model for P_n prediction but is within the GT10 threshold at three stations, SANG, AMDO, and ERDO, for all three period bands. FW is too slow for the other four stations in all periods. While LITHO1.0 and RSTT are generally within the GT10 threshold at 2–10 s period, in spite of being slightly fast, they become too fast at shorter periods at many stations. All models have negative Δs at station TUNL (at the southern edge of the Qaidam Basin), suggesting that V_p of the mantle beneath the Qaidam Basin may be too slow in all the six models.

5.2. Event 1999087: Earthquake

Similar to the performance of the models in predicting Rayleigh waves from the explosion, all the models inverted from surface wave data produce better Rayleigh phase predictions than the models based on *P* wave

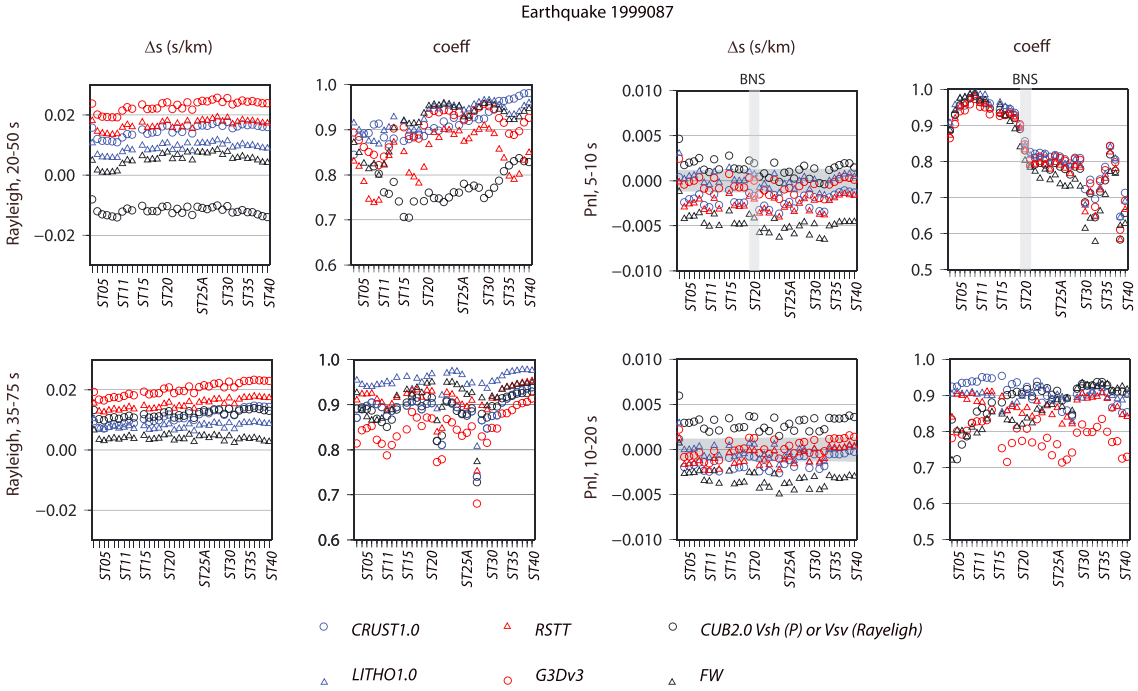

Figure 10. Slowness perturbations (Δs) and cross-correlation coefficients for Event 1999087. Δs and correlation coefficients of (first and second columns) Rayleigh waves and (third and fourth columns) P_{nl}. Figure 10 (first and second columns) is for Rayleigh waves at periods of (top) 20–50 s and (bottom) 35–75 s; Figure 10 (third and fourth columns) is for P_n/P_{nl} waves at periods of (top) 5–10 s and (bottom) 10–20 s. The stations are listed along the profile from south to north. The location where the profile crossed the BNS is around station ST20. For P_{nl} at 5–10 s period, a steep offset in correlation coefficients is observed at the BNS (gray area, top right), associated with a sudden north-to-south change in P_{nl} waveforms (see supporting information Figure S3).

data (Figure 10 and Table 3). The full-waveform-based model FW yields the smallest $|\Delta s|$ in both period bands of regional Rayleigh waves. Also, CUB2.0-V_{sv} is too slow in the crust but too fast in deeper depths, because of negative Δs at 20–50 s period and positive Δs at 35–75 s period throughout the INDEPTH-III profile.

For P_{nl} waves at 5–10 s periods, the six models yield relatively coherent patterns of Δs. The models can be ordered as CUB2.0 (V_{sh}) > LITHO1.0 > G3Dv3 > CRUST1.0 > RSTT > FW from fast to slow for all stations. CUB2.0-V_{sh} generally produces faster predictions than observed arrivals. The model yielding overall the smallest slowness perturbation is LITHO1.0. At 10–20 s periods, the fast-slow ordered list is generally similar to that of 5–10 s periodsfor the southernmost stations, except that RSTT is faster than CRUST1.0. Moving to the north, G3Dv3 becomes faster than LITHO1.0 after station ST15, and RSTT and LITHO1.0 tend to give the same predictions of Δs at the northern end of the profile. We count the number of stations for which the model prediction is within the GT10 threshold for this earthquake (Table 5), which suggests that LITHO1.0 and G3Dv3 are the models performing the best for P_{nl} at 5–20 s periods. CUB2.0 (V_{sh}) performs well for the stations in the north at 5–10 s periods but becomes too fast

Table 5. A Summary of the Number of Stations Where a Given Model is Located Within the GT10 Threshold for P_{nl} From Earthquake 1999087[a]

	5–10 s P_{nl}		10–20 s P_{nl}	
Model	XR-South (Lhasa)	XR-North (Qiangtang)	XR-South (Lhasa)	XR-North (Qiangtang)
CRUST1.0	2	0	4	11
LITHO1.0	13	17	14	16
RSTT	1	0	4	14
G3Dv3	14	13	12	18
CUB2.0 (V_{sh})	1	12	0	0
FW	1	0	1	0

[a]Same as Table 3, XR-South and XR-North represent the INDEPTH-III stations on each side of the BNS. The total station number is 36, including 16 stations in the south and 20 stations in the north.

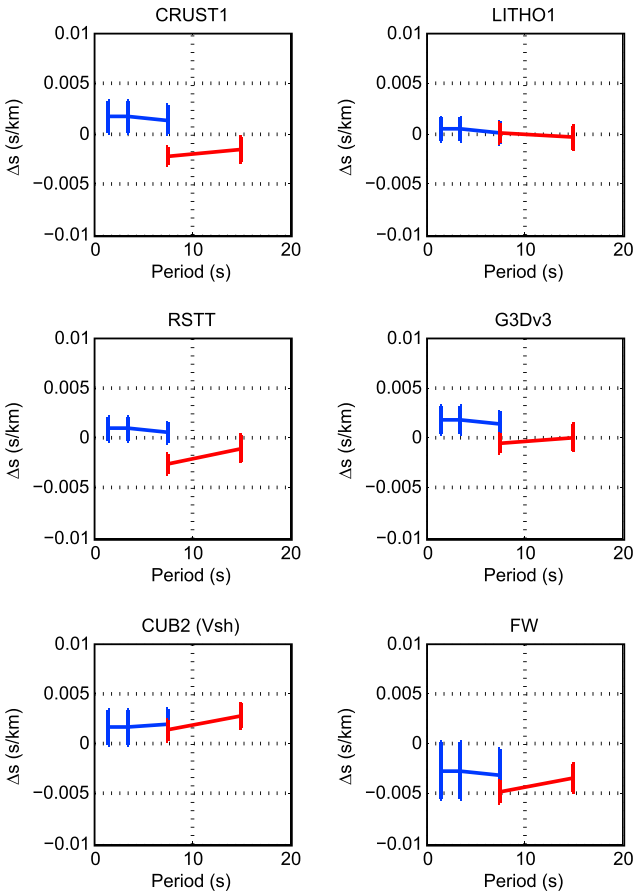

Figure 11. The change of P_n/P_{nl} slowness perturbation (Δs) with period for each model. The 1σ error bars of the measurements at each period are shown in blue and red for Event 1992142 and Event 1999087, respectively. The period where an error bar locates represents the central period of each period band, such as 7.5 s for the period band of 5–10 s.

at longer periods; in contrast, RSTT performs better at 10–20 s periods (especially at the northern end of the profile) but is too slow at shorter periods. The frequency dependence of Δs for P_n/P_{nl} is again observed here (Figure 11, red lines).

It is worth mentioning that the BNS, which is highlighted as the shaded area in Figure 10, marks a sharp boundary in the cross-correlation coefficients for P_{nl} waves of 5–10 s periods. To the south of the BNS, more than 95% measurements of correlation coefficients are larger than 0.9. In contrast, the values of correlation coefficient dramatically decrease to the north of the BNS, with none of the coefficients exceeding 0.88 for those northern stations. This sudden transition is observed for all six models. A close comparison of the P_{nl} waveforms at stations just south and north of the BNS (ST15 and ST20, Figure S3) reveals that the variation in correlation coefficients is possibly associated with the sudden change in waveforms near the end of the phase windows (the right solid blue lines). None of the six models can predict the small wiggles behind the main peak of P_n observed in the northern stations. The largest Moho offset in Tibet, of up to 10 km, may locate along the BNS [e.g., *Griffin et al.*, 2011]. This waveform change is presumably due to unmodeled Moho undulation, doublet Moho [e.g., *Nabelek et al.*, 2009], and/or thin layers in the mantle lid. This phenomenon is not observed in the correlation coefficients of P_{nl} waves at longer periods.

6. Discussion

6.1. Frequency Dependence of P_n/P_{nl}

The time differences between the observation and the synthetics change slightly with period, indicating that the validation of a model is weakly frequency dependent (Figure 11). In most cases, the predicted Δs of P_n/P_{nl} tends to decrease when the period increases from 1 to ~10 s and increase above ~10 s period. Two exceptions are CUB2.0 (V_{sh}), which shows a monotonic increase of Δs with period, and LITHO1.0, which shows a monotonic decrease of Δs with period.

The relative increase in the predicted velocity of P_n at long periods could be attributed to the vertical velocity gradient. *Zhang et al.* [2007] showed that Fréchet kernels of P_n actually include a volume along and around the classic ray path. *Zhang et al.* [2007] also simulated local P_n waves in a model including a mantle layer with a uniformly positive velocity gradient overlaid by a crustal layer and showed that a velocity gradient of 0.02 (km/s)/km can cause an increase in Δs of 0.0012 s/km at a distance of ~100 km when the period increases from 1 to 5 s, compared to the value for a model with a homogeneous mantle. Previous seismic studies have suggested widespread positive velocity gradients in the Tibetan mantle [e.g., *Holt and Wallace*, 1990; *Phillips et al.*, 2007;

Lü et al., 2014]. The velocity gradient in the mantle of RSTT is typically smaller than 0.002 (km/s)/km beneath Tibet. This may explain that at periods longer than 5 s, the increase in Δs with period for RSTT is more than that for CRUST1.0, which does not have any vertical gradient in the mantle lid. In contrast, negative velocity gradients are found in the mantle of LITHO1.0 and G3Dv3 beneath Tibet and surrounding regions. This is consistent with our observation in Figure 11, where there is no or little relative increase in the predicted velocity of P_n for LITHO1.0 and G3Dv3 between 5 and 20 s periods. Negative velocity gradients may occur in the mantle except Precambrian shields and old platforms and may cause complicated dispersion of P_n waves [*Tittgemeyer et al.*, 2000].

In our study, the frequency dependency of the P_n/P_{nl} phase perturbation typically causes change in Δs of ~0.001 s/km for the periods of 1–10 s and $<$ 0.002 s/km for the periods of 5–20 s, indicating insignificant "relative dispersion" of the P_n/P_{nl} phase. This is worth noting, particularly for future full-wave tomography that depends on 3-D waveform simulation, as it indicates that models constructed from intermediate-period P_n waves may be employed to predict short-period P_n traveltimes.

6.2. Lateral Variations in Model Prediction

6.2.1. Rayleigh Waves

FW is overall the best matching model for regional Rayleigh waves (Table 3). This suggests that models inverted from full-wave tomography and 3-D forward modeling improve the prediction of wave propagation. We emphasize that all the data used in this validation were not included in the generation of FW, which is based on ambient noise data. For the Rayleigh waves from the explosion, FW is slightly fast for the stations SANG and AMDO located in the Lhasa terrane and slow for the station MAQI in the eastern Tibet. For the earthquake sending Rayleigh waves from nearly southwest, FW is fast for the stations located in the Lhasa and Qiangtang terrane. Although FW is the best matching model for Rayleigh waves in the whole region, it is slightly fast in V_{sv} in the western part of the study area but slightly slow in the east.

LITHO1.0 also performs well with predictions close to those from FW, though it is faster. CUB2.0-V_{sv} is slow in the crust but probably fast in the mantle, which causes a very negative Δs at 20–50 s period but close-to-zero Δs at 35–75 s period for both events.

6.2.2. P_n/P_{nl} Waves

For the stations in the Lhasa terrane and the Qiangtang terrane, FW is an overall GT10 model for 1–10 s period P_n/P_{nl} traveling from the explosion to stations SANG and AMDO. RSTT and LITHO1.0 are also GT10 models for these two stations at the periods of 2–10 s. At 5–10 s, LITHO1.0 is a GT10 model for station ERDO as well as FW. In contrast, the predictions from LITHO1.0, G3Dv3, and CUB2.0-V_{sh} fit the observations significantly better than FW at longer periods for the earthquake. LITHO1.0 is typically one of the GT10 models for station AMDO and the XR-South stations, which are separated by about 100 km. Neither FW nor RSTT performs well for XR stations. FW typically produces a slow arrival with an average Δs of ~0.005 s/km at 5–10 s period, which means ~5 s phase time delays at the stations; RSTT similarly yields an average Δs of ~0.003 s/km. The significant failure of FW and RSTT for Event 1999087 is not caused by the frequency dependency discussed in section 6.1, since both FW and RSTT are actually GT10 models for Event 1992142 at the same period band and station AMDO. Uncertainty in the source location estimation may cause up to 1.26 s error in P_n waves as estimated in section 4.2, which does not fully explain this large phase delay measurements for the two models. An early/late rise in the source time function of the earthquake relative to that used in simulation could lead to a later/earlier phase in synthetics. It is also likely that the difference in the performances of these models is mainly caused by the spatial variation in the model validity.

The Songpan-Ganzi terrane consists of the northern edge and the northeastern corner of the plateau. We can only validate the models of this terrane (the Qaidam Basin as well) by using the data of explosion Event 1992142 from which all waves propagated from the northwest. The three available stations are widely distributed within the terrane with largely varying source-receiver paths. The best matching models vary at different stations and periods, but LITHO1.0 and RSTT remain in the GT10 threshold at more stations than other models. Being a typically slow model, FW disappears in the GT10 model list for the stations located in this terrane.

For the station in the Qaidam Basin, TUNL, the prediction of P_n arrivals from G3Dv3matches observations well, as well as CRUST1.0 and RSTT. The typically observed negative Δs at station TUNL may indicate that the V_p of the mantle beneath the Qaidam Basin is too slow. The source-receiver paths for the station USHU in the

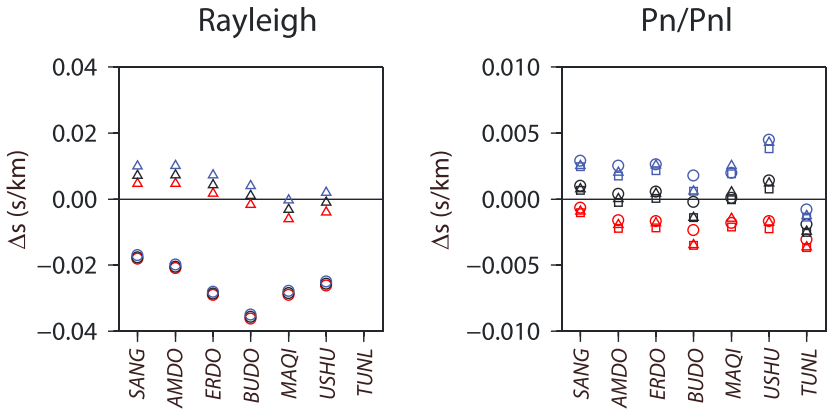

Figure 12. Slowness perturbations (Δs) for Event 1992142 from the three parameters in CUB2.0, V_{sv} (red), V_{sh} (blue), and Voigt average V_s (black). (left) Rayleigh waves and (right) P_n/P_{nl} waves. For Rayleigh waves, the measurements at periods of 20–50 s and 35–75 s are shown as circles and triangles, respectively. For P_n/P_{nl}, the measurements at periods of 5–10 s, 2–5 s, and 1–2 s are shown as circles, triangles, and squares, respectively. Same as Figure 9, the measurements of Rayleigh waves at station TUNL are not involved because of poor signals.

Songpan-Ganzi terrane traveled through TUNL approximately, where significantly positive Δs is observed at USHU from G3Dv3. This large shift between TUNL and USHU, of ~0.003 s/km, is also found for all other models. For a model showing positive Δs at USHU, such as G3Dv3, V_p in the mantle between these two stations may be too fast in the model.

Though usually not the best matching model, LITHO1.0 shows a relatively good and stable performance in predicting both Rayleigh waves and P_n/P_{nl} waves throughout the study area, especially for the paths from the southwest (Event 1999087). RSTT is one of the best fitting models for P_n/P_{nl} waves at many stations for the paths from the north (Event 1992142). This is presumably because the propagation of P_n was carefully treated in RSTT by including the effect of a positive velocity gradient. However, RSTT does not predict significantly better P_n/P_{nl} waves than some models only inverted from surface waves, such as LITHO1.0 and FW, probably because the uniform velocity gradient for the whole upper mantle is too simple. Also, RSTT yields poor predictions of Rayleigh waves, for which V_s in the Tibetan crust and upper mantle of RSTT may be too fast.

6.3. Effects of Radial Anisotropy

The uppermost mantle is radially anisotropic. While long-period Rayleigh wave phase velocity is mainly sensitive to V_{sv}, P_n travels nearly horizontally in the uppermost mantle and thus is mostly sensitive to V_{ph} in the upper mantle. To get a sense of the magnitude of the effects of radial anisotropy on Rayleigh and P_n/P_{nl}, we estimate the influence of radial anisotropy by using the model CUB2.0, which provides estimations of V_{sv}, V_{sh}, and Voigt average V_s. We employ the V_p/V_s ratio of AK135 to convert *S* wave velocity to *P* wave velocity. The synthetic Rayleigh and P_n/P_{nl} waves predicted from the three models, CUB2.0 (V_{pv}, V_{sv}), CUB2.0 (V_{ph}, V_{sh}), and CUB2.0 (Voigt V_p, Voigt V_s), are thus compared for Event 1992142 (Figure 12).

As expected, the predicted phase arrivals from V_{sv} and V_{sh} are the slowest and the fastest, respectively. In Tibet, Rayleigh waves of 20–50 s period mainly sample the crustal structures, so that there is no significant difference in the predictions from the three models for this period band (V_{sv} and V_{sh} differ only in the mantle in CUB2.0). In contrast, for Rayleigh waves of 35–75 s period, which samples more upper mantle structures, the predictions of Δs differ by ~0.007 s/km between V_{sv} and V_{sh} models, which are larger than the difference in the predictions from LITHO1.0, CUB2.0 (V_{sv}), and FW. The influence of radial anisotropy is also pronounced for P_n/P_{nl} waves. For example, at station AMDO and periods of 2–5 s, CUB2.0 (V_{ph}, V_{sh}) is a fast model with Δs of ~0.002 s/km, but CUB2.0 (V_{pv}, V_{sv}) is a slow model with Δs of ~ −0.002 s/km. The Voigt average model yields a better match than the anisotropic models. This does not mean that radial anisotropy should be ignored, because theoretically P_n should propagate around the speed of V_{ph}. On the contrary, it indicates that the *P* wave velocity (V_{ph}) converted from shear velocity in CUB2.0 is too fast, assuming the V_p/V_s ratio in our treatment is correct. This is consistent with our observation from 35–75 s period Rayleigh waves for the stations in the Lhasa terrane and the

Qiangtang terrane. For the stations in the Songpan-Ganzi terrane, especially MAQI and USHU in eastern Tibet, CUB2.0 is a slow V_{sv} model for Rayleigh waves but a fast V_{ph} model for P_n/P_{nl} waves.

The presence of radial anisotropy may also provide an explanation for the discrepancy in FW, which yields good predictions for Rayleigh waves but late P_n/P_{nl} arrivals. Since FW is generated based on Rayleigh waveforms extracted from ambient noise, its V_s and V_p represent V_{sv} and V_{pv}, respectively. Since V_{pv} is generally smaller than V_{ph} in the uppermost mantle, it is expected that the predicted P_n/P_{nl} waves are slow.

7. Conclusion

High-resolution tomographic models are essential for understanding the physical and compositional properties in the lithosphere and obtaining accurate earthquake source locations and moment tensors. Yet, there are significant disagreements in recent three-dimensional velocity models of the crust and uppermost mantle in Tibet. The question also remains as to whether models constructed from one type of seismic waves (body or surface waves) can be used to predict traveltimes and waveforms of another. In this study, we simulate waveforms from six recent 3-D global or regional Earth models for Tibet and the vicinity. We select GT events located in regional distances as the sources, which include one explosion and one natural earthquake. A 3-D finite-difference method in the spherical coordinates is used to simulate regional seismic waveforms with frequencies up to 1 Hz. Synthetic waveforms of 20–75 s period Rayleigh waves and 1–20 s period P_n (or P_{nl}) waves are compared to the corresponding observed waveforms. The phase delays and correlation coefficients are measured for both Rayleigh and P_n/P_{nl} waves at different period bands. In general, the slowness perturbation, converted from the phase delay, is considered as the primary factor in the validation.

FW, constructed from full-wave ambient noise tomography as well as 3-D waveform modeling, typically produces the best predictions of Rayleigh waves traveling within the study area, where the data for validation were not involved in the model generation. This result highlights the value of utilizing the full-wave theory to improve the accuracy and resolution of seismic tomographic models. The best model for P_n/P_{nl} predictions is laterally varying and weakly frequency dependent. For P_n/P_{nl} arrival times, FW, LITHO1.0, and RSTT yield good predictions for the paths traveling in central Tibet, while FW is too slow for the paths traveling in eastern and western Tibet. LITHO1.0, which is an isotropic model generated from only surface wave data by assuming a V_p/V_s ratio fixed within each layer, shows a relatively good and stable performance in predictions for both P_n/P_{nl} and Rayleigh waves. We conclude that none of the six models provides a satisfactory match for both P_n/P_{nl} and Rayleigh waves that are within the observation errors. This is possibly mainly due to lack of accurate constraints on radial anisotropy and V_p/V_s ratios in the upper mantle. Although strong crustal anisotropy and azimuthal anisotropy have also been observed in Tibet [*Ozacar and Zandt*, 2004; *Duret et al*., 2010], we are not able to assess their effects in wave prediction since they are not included in any of the candidate models.

We emphasize that our objective is not to rank the models but to investigate the possible discrepancies between observations and the predictions from different Earth models, from which we could identify the need for model improvement. Our study strongly suggests the need for an integrated velocity model constructed with multiple seismic waveforms and consideration of anisotropy in order to simultaneously describe *P*, *S*, and surface waves.

Acknowledgments

All the waveform data are requested from the IRIS Data Management Center. The GT event source parameters are obtained from the International Seismological Centre (http://www.isc.ac.uk/) and the global CMT solutions (http://www.globalcmt.org). The model CRUST1.0 is available at the IRIS EMC-Reference Models (https://ds.iris.edu/ds/products/emc-referencemodels/). The model LITHO1.0 is downloaded from igppweb.ucsd.edu/~gabi/litho1.0.html. The model RSTT is available at www.sandia.gov/rstt. The model LLNL-G3Dv3 is available at the IRIS EMC-Earth Models (https://ds.iris.edu/ds/products/emc-earthmodels/). The upper mantle shear velocity model CUB2.0 is available at ciei.colorado.edu/~nshapiro/MODEL/. The models CRUST2.0 [*Bassin et al*., 2000] and S362ANI [*Kustowski et al*., 2008] used in the waveform comparison discussed in the supporting information are downloaded from https://ds.iris.edu/ds/products/emc-referencemodels/ and https://ds.iris.edu/ds/products/emc-earthmodels/. We thank all the authors who made their models publically available. TauP Toolkit for estimating P_n arrival time in this study is available at www.seis.sc.edu/taup/. We thank Sandy Ballard for his help in extracting the 3-D Earth model RSTT and Nian Wang for helpful discussions. We thank two anonymous reviewers for their careful and constructive comments. This research is supported by the Air Force Research Laboratory (award FA9453-13-C-0362).

References

Bassin, C., G. Laske, and G. Masters (2000), The current limits of resolution for surface wave tomography in North America, *EOS Trans AGU, 81*, F897.

Bondár, I., S. C. Myers, R. Engdahl, and E. A. Bergman (2004), Epicenter accuracy based on seismic network criteria, *Geophys. J. Int.*, *156*, 483–496, doi:10.1111/j.1365-246X.2004.02070.x.

Brocher, T. M. (2005), Empirical relations between elastic wave speeds and density in the Earth's crust, *Bull. Seismol. Soc. Am.*, *95*(6), 2081–2092, doi:10.1785/0120050077.

Christensen, N. I., and W. D. Mooney (1995), Seismic velocity structure and composition of the continental crust: A global view, *J. Geophys. Res.*, *100*, 9761–9788, doi:10.1029/95JB00259.

Crotwell, H. P., T. J. Owens, and J. Ritsema (1999), The TauP Toolkit: Flexible seismic travel-time and ray-path utilities, *Seismol. Res. Lett.*, *70*, 154–160.

Duret, F., N. M. Shapiro, Z. Cao, V. Levin, P. Molnar, and S. Roecker (2010), Surface wave dispersion across Tibet: Direct evidence for radial anisotropy in the crust, *Geophys. Res. Lett.*, *37*, L16306, doi:10.1029/2010GL043811.

Ekström, G., M. Nettles, and A. M. Dziewonski (2012), The global CMT project 2004–2010: Centroid-moment tensors for 13,017 earthquakes, *Phys. Earth Planet. Inter.*, *200-201*, 1–9, doi:10.1016/j.pepi.2012.04.002.

Gao, H., and Y. Shen (2012), Validation of shear-wave velocity models of the Pacific Northwest, *Bull. Seismol. Soc. Am.*, *102*(6), 2611–2621, doi:10.1785/0120110336.

Gao, H., and Y. Shen (2015), Validation of recent shear wave velocity models in the United States with full-wave simulation, *J. Geophys. Res. Solid Earth*, *120*, 344–358, doi:10.1002/2014JB011369.

Griffin, J. D., R. L. Nowack, W.-P. Chen, and T.-L. Tseng (2011), Velocity structure of the Tibetan lithosphere: Constraints from *P*-wave travel times of regional earthquakes, *Bull. Seismol. Soc. Am.*, *101*, 1938–1947, doi:10.1785/0120100229.

He, R., X. Shang, C. Yu, H. Zhang, and R. D. Van der Hilst (2014), A unified map of Moho depth and V_p/V_s ratio of continental China by receiver function analysis, *Geophys. J. Int.*, *199*, 1910–1918, doi:10.1093/gji/ggu365.

Holt, W. E., and T. C. Wallace (1990), Crustal thickness and upper mantle velocities in the Tibetan Plateau Region from the inversion of regional P_{nl} waveforms: Evidence for a thick upper mantle lid beneath southern Tibet, *J. Geophys. Res.*, *95*, 12,499–12,525, doi:10.1029/JB095iB08p12499.

Kennett, B. L. N., E. R. Engdahl, and R. Buland (1995), Constraints on seismic velocities in the Earth from travel times, *Geophys. J. Int.*, *122*, 108–124.

Komatitsch, D., and J. Tromp (2002), Spectral-element simulations of global seismic wave propagation-II, 3-D models, oceans, rotation, and self-gravitation, *Geophys. J. Int.*, *150*(1), 303–318, doi:10.1046/j.1365-246X.2002.01716.x.

Kustowski, B., G. Ekström, and A. M. Dziewoński (2008), Anisotropic shear-wave velocity structure of the Earth's mantle: A global model, *J. Geophys. Res.*, *113*, B06306, doi:10.1029/2007JB005169.

Laske, G., G. Masters, Z. Ma, and M. Pasyanos (2013), Update on CRUST1.0—A 1-degree global model of Earth's crust Geophys. Res. Abstracts, 15, Abstract EGU2013-2658.

Lee, E.-J., P. Chen, and T. H. Jordan (2014), Testing waveform predictions of 3D velocity models against two recent Los Angeles earthquakes, *Seismol. Res. Lett.*, *85*(6), 1275–1284, doi:10.1785/0220140093.

Li, Y., M. Gao, and Q. Wu (2014), Crustal thickness map of the Chinese mainland from teleseismic receiver functions, *Techtonophysics*, *611*, 51–60, doi:10.1016/j.tecto.2013.11.019.

Lü, Y., Z. Zhang, S. Pei, E. Sandvol, T. Xu, and X. Liang (2014), 2.5-Dimensional tomography of uppermost mantle beneath Sichuan-Yunnan and surrounding regions, *Tectonophysics*, *627*, 193–204, doi:10.1016/j.tecto.2013.03.008.

Maceira, M., C. Larmat, R. W. Porritt, D. M. Higdon, C. A. Rowe, and R. M. Allen (2015), On the validation of seismic imaging methods: Finite frequency or ray theory?, *Geophys. Res. Lett.*, *42*, 323–330, doi:10.1002/2014GL062571.

Myers, S. C., et al. (2010), A crust and upper-mantle model of Eurasia and North Africa for P_n travel-time calculation, *Bull. Seismol. Soc. Am.*, *100*, 640–656, doi:10.1785/0120090198.

Myers, S. C., N. A. Simmons, G. Johannesson, and E. Matzel (2015), Improved regional and teleseismic *P*-wave travel time prediction and event location using a global 3D velocity model, *Bull. Seismol. Soc. Am.*, *105*, 1642–1660, doi:10.1785/0120140272.

Nabelek, J., G. Hetenyi, J. Vergne, S. Sapkota, B. Kafle, M. Jiang, H. Su, J. Chen, B.-S. Huang, and the HI-CLIMB team (2009), Underplating in the Himalaya-Tibet collision zone revealed by the Hi-CLIMB experiment, *Science*, *325*, 1371–1374, doi:10.1126/science.1167719.

Ozacar, A. A., and G. Zandt (2004), Crustal seismic anisotropy in central Tibet: Implications for deformational style and flow in the crust, *Geophys. Res. Lett.*, *31*, L23601, doi:10.1029/2004GL021096.

Pasyanos, M. E., T. G. Masters, G. Laske, and Z. Ma (2014), LITHO1.0: An updated crust and lithospheric model of the Earth, *J. Geophys. Res. Solid Earth*, *119*, 2153–2173, doi:10.1002/2013JB010626.

Phillips, W. S., M. L. Begnaud, C. A. Rowe, L. K. Steck, S. C. Myers, M. E. Paysanos, and S. Ballard (2007), Accounting for lateral variations of the upper mantle gradient in P_n tomography studies, *Geophys. Res. Lett.*, *34*, L14312, doi:10.1029/2007GL029338.

Ritzwoller, M. H., N. M. Shapiro, M. P. Barmin, and A. L. Levshin (2002), Global surface wave diffraction tomography, *J. Geophys. Res.*, *107*(B12), 2335, doi:10.1029/2002JB001777.

Rodgers, A. J., N. A. Petersson, and B. Sjogreen (2010), Simulation of topographic effects on seismic waves from shallow explosions near the North Korean nuclear test site with emphasis on shear wave generation, *J. Geophys. Res.*, *115*, B11309, doi:10.1029/2010JB007707.

Satyabala, S. P., and R. Bilham (2006), Surface deformation and subsurface slip of the 28 March 1999 $M_w = 6.4$ west Himalayan Chamoli earthquake from InSAR analysis, *Geophys. Res. Lett.*, *33*, L23305, doi:10.1029/2006GL027422.

Shapiro, N. M., and M. H. Ritzwoller (2002), Monte Carlo inversion for a global shear velocity model of the crust and upper mantle, *Geophys. J. Int.*, *151*, 88–105, doi:10.1046/j.1365-246X.2002.01742.x.

Shen, Y., and W. Zhang (2012), Full-wave tomography of the Eastern Hemisphere, in *Proceedings of the 2012 Monitoring Research Review: Ground-Based Nuclear Explosion Monitoring Technologies*, pp. 121–129, Albuquerque, NM.

Shen, Y., Y. Ren, H. Gao, and B. Savage (2012), An improved method to extract very-broadband empirical Green's functions from ambient seismic noise, *Bull. Seismol. Soc. Am.*, *102*(4), 1872–1877, doi:10.1785/0120120023.

Simmons, N. A., S. C. Myers, G. Johannesson, and E. Matzel (2012), LLNL-G3Dv3: Global *P* wave tomography model for improved regional and teleseismic travel time prediction, *J. Geophys. Res.*, *117*, B10302, doi:10.1029/2012JB009525.

Song, T.-R. A., and D. V. Helmberger (2007), Validating tomographic models with broad-band waveform modeling: An example from the LA RISTRA transect in the southwestern United States, *Geophys. J. Int.*, *171*, 244–258, doi:10.1111/j.1365-246X.2007.03508.x.

Tittgemeyer, M., F. Wenzel, and K. Fuchs (2000), On the nature of P_n, *J. Geophys. Res.*, *105*, 16,173–16,180, doi:10.1029/2000JB900061.

Tromp, J., et al. (2010), Near real-time simulations of global CMT earthquakes, *Geophys. J. Int.*, *183*, 381–389, doi:10.1111/j.1365-246X.2010.04734.x.

Zhang, W., Y. Shen, and L. Zhao (2012), Three-dimensional anisotropic seismic wave modeling in spherical coordinate by a collocated-grid finite difference method, *Geophys. J. Int.*, *188*, 1359–1381, doi:10.1111/j.1365-246X.2011.05331.x.

Zhang, Z., Y. Shen, and L. Zhao (2007), Finite-frequency sensitivity kernels for head waves, *Geophys. J. Int.*, *171*, 847–856, doi:10.1111/j.1365.246X.2007.03575.x.

Zhao, L.-S., and J. Xie (1993), Lateral variations in compressional velocities beneath the Tibetan Plateau from P_n travel time tomography, *Geophys. J. Int.*, *115*, 1070–1084.